

Simultaneous particle-image velocimetry–planar laser-induced fluorescence measurements of Richtmyer–Meshkov instability growth in a gas curtain with and without reshock

B. J. Balakumar,^{a)} G. C. Orlicz, C. D. Tomkins, and K. P. Prestridge

Physics Division, Los Alamos National Laboratory, Los Alamos, New Mexico 87545, USA

(Received 13 May 2008; accepted 15 October 2008; published online 15 December 2008)

The structure of the concentration and velocity fields in a light-heavy-light fluid layer subjected to an impulsive acceleration by a shock wave (Richtmyer–Meshkov instability) is studied using simultaneous particle-image velocimetry and planar laser-induced fluorescence (PLIF) measurements (performed in such flows for the first time). The initial condition prior to shock impact is accurately characterized using calibrated PLIF measurements to enable comparisons of the evolving structure to numerical simulations. Experiments performed on a SF₆ curtain in air (Atwood number, $At=0.67$), after single shock by a Mach 1.2 shock wave and reshock by the reflected wave, show that the reshock wave has a dramatic impact on the evolution of the unstable structure. After first shock and in the absence of reshock(s), the structure widths agree well with an analytical extension to the nonlinear point vortex model [J. W. Jacobs *et al.*, “Nonlinear growth of the shock-accelerated instability of a thin fluid layer,” *J. Fluid Mech.* **295**, 23 (1995)] that accounts for the nonuniform spacing of the row of counter-rotating vortices that drive the flow. However, upon reshock, the width deviates significantly from the singly shocked case, and a substantial rise in the growth rate is observed. Enhanced mixing, destruction of the ordered velocity field, and an increase in both the positive and negative circulations ensue. Large velocity fluctuations relative to the mean flow, and the advection of a wide spectrum of vortex scales combine to mix the flow well and create turbulent conditions in the reshocked structure. © 2008 American Institute of Physics.

[DOI: [10.1063/1.3041705](https://doi.org/10.1063/1.3041705)]

I. INTRODUCTION

The amplification of perturbations at an impulsively accelerated density gradient is called the Richtmyer–Meshkov (RM) instability. The RM instability is created by the deposition of baroclinic vorticity at the density gradient interface due to the misalignment of pressure and density gradients. A significant amount of research has been invested into the study of the classical single interface development (Brouillette and Sturtevant,^{1,2} Jacobs and Sheeley,³ Puranik,⁴ among others). While the canonical problem might be useful to understand the physics of the RM instability, real-life instances in applications such as inertial confinement fusion,⁵ supersonic engines,⁶ and supernova explosions⁷ involve fluid layers of finite thickness.⁸ Finite-thickness layers (e.g., gas curtain) also exhibit a richer array of behavior compared to the single interface. Phenomena such as freeze-out, interface coupling, and feedthrough are unique to fluid layers subjected to RM instability. A gas curtain also allows the possibility of creating initial flow configurations and initial modal compositions that are difficult to achieve in membraneless single interface configurations.

The first RM experiments on membraneless gas curtains in a configuration similar to the present experiments were reported by Jacobs *et al.*⁹ Using a gravity-driven SF₆ gas curtain, and a Mach 1.2 shock wave, they observed three distinct types of patterns during the intermediate growth

stage—the upstream mushroom, the sinuous, and the downstream mushroom patterns. It was conjectured that small variations in the initial vorticity deposition by the first shock created the differences observed at intermediate time. Using planar laser Rayleigh scattering, it was confirmed by Budzinski *et al.*¹⁰ that differences in initial perturbation amplitudes between the two edges of the curtain resulted in the development of the three flow patterns. Further, a correlation of the initial conditions with the intermediate flow pattern showed that the ratio between the upstream and downstream amplitudes in the initial condition determined the pattern that eventually formed.¹¹ Upstream patterns appeared when the ratio was larger than 1.2, downstream patterns formed when the ratio was less than 0.3, and the sinuous modes appeared for values between 0.3 and 1.2. These differing patterns were also observed in the two-dimensional simulations performed using the CALE hydrocode, when the simulations reflected the initial conditions in the experiments.⁸

Analytical growth rate models are limited in number for the gas curtain (in contrast to the single interface case). Mikaelian¹² derived the linear growth rate of perturbations on the surface of a curtain under the assumption of incompressibility following a prescription similar to that given by Richtmyer.¹³ The nonlinear growth at later times was derived using a point vortex model assuming uniformly spaced counter-rotating vortices by Jacobs *et al.*¹⁴ While large initial perturbation amplitudes [$ka_0 \sim O(1)$], where k is the perturbation wavenumber and a_0 is the initial amplitude), such as

^{a)}Electronic mail: bbalasub@lanl.gov.

those present in the experiments mentioned here, reduce the duration of the linear growth regime making model validation in the linear regime difficult, the predictions of the models in the nonlinear regime have been compared to experimental data in the past.¹⁴

Attempts to simulate the gas curtain experiments using numerical codes have yielded mixed results. Simulation results from the AMR code RAGE by Baltrusaitis *et al.*¹⁵ showed a qualitative agreement of the larger scales, but growth rate differences of 5%–10% depending on whether the simulations were performed in a center of mass frame or the laboratory frame. *Preshock waves* (small pressure gradients in the shock tube that precede the main shock wave due to improper bursting of the diaphragm) were found to easily turn sinusoidal structures into upstream mushrooms, pointing to the importance of eliminating preshocks in experiments. Numerical simulations using CALE were performed by Mikaelian¹⁶ using experimental data from gas curtains, with and without reshock. It was found that the large-scale structures agreed well with the experiments in a qualitative sense. Reshock simulations and simulations using a sinusoidal initial layer were also performed but not validated due to the absence of experimental data. While the large-scale structures in the simulations qualitatively agree with the experiments at early times, accurate prediction of the small-scale structures remains elusive.

The small-scale structures in the experimental results of Rightley *et al.*¹⁷ were compared to RAGE and CUERVO simulations in Rider *et al.*¹⁸ and Rider *et al.*¹⁹ Significant variations in the spectral signatures were found between the simulations and the experiments. While the high-resolution shock capturing schemes exhibited a behavior qualitatively similar to the data, results using first-order methods showed closer agreement both qualitatively and quantitatively (i.e., using fractal dimension calculations and wavelet transform spectra). Based on these results, the simulation of gas curtains, especially at later times, remains a challenging problem despite advances in numerical techniques. In part, this is attributable to the lack of high-quality validation data from well-controlled experiments that can be used to diagnose the simulations.

Several aspects concerning the mixing of gas curtains at late times, and the subsequent transition to turbulence, also remain unresolved. It was observed that the mixing width of the structure saturated in the case of a moderately perturbed varicose curtain but no saturation was present for more severe perturbations.²⁰ Later, Vorobieff *et al.*²¹ showed that the intensity structure function reached a $-5/3$ slope for the multimode instability for correlations at small distances, pointing to a transition to turbulence. A mixing transition was also observed by Rightley *et al.*¹⁷ and Vorobieff *et al.*²² using wavelet transforms, histogram analysis, and the calculation of fractal dimensions. A method to further investigate these phenomena was provided by the application of particle-image velocimetry (PIV) measurements in RM flows by Prestridge *et al.*²³

While each of these experiments represented interesting developments in the study of RM instabilities, they also suffered from a fundamental problem—the experiments were

performed on a gas curtain that was initially unstable. The instability of the gas curtain manifested itself in minor variations in the initial conditions that were significant enough to create dramatic changes in the postshock behavior. This problem assumes additional significance in the study of reshock statistics. Turbulence statistics calculated on a flow whose mean varies significantly may be subject to large bias errors. This effect is expected to be prominent for RM-unstable flows as small changes in the structure at the time of reshock result in entirely different vorticity deposition patterns upon reshock. The current experiment eliminates the problem of an unstable curtain by modifying the nozzle configuration used in the previous experiments to create a passive coflow configuration that is significantly more stable. With the present initial conditions, only the sinuous mode of development is observed commensurate with a symmetric curtain. This stable curtain allows the meaningful comparison of independent realizations obtained at different times, to enable the construction of an ensemble of related data and ultimately, the quantitative estimation of turbulence statistics after reshock to answer important questions regarding the stability of statistics, mixing, and transition to turbulence.

The study of reshock and the subsequent production or modulation of turbulence assumes importance in applications such as inertial confinement fusion, where reshocks cannot be avoided due to the spherical geometry. Reshocks deposit additional energy into an already RM-unstable structure, promoting the dispersion of energy into a wide spectrum of scales. This is particularly desirable for repeatable, diffuse curtains at low Mach numbers (such as the present experiments), where a ready transition to turbulence is not observed after a single shock. Thus, a forced transition to turbulence by means of a reshock mechanism allows the capture of true ensemble averaged turbulence statistics that can then be used for the development of closure models for variable density turbulent flows. A considerable amount of research has been expended toward the study of reshock effects on the widths and growth rates of single interfaces excited by multiple shock waves (Brouillette and Sturtevant,^{1,2} Zaitsev *et al.*,²⁴ Brouillette and Sturtevant,²⁵ for example) but reshock experiments on fluids layers remain scarce. Efforts to measure the turbulent fluctuation statistics of the mixing zone induced by the RM instability have been generally limited to turbulent velocity or concentration statistics using thermal anemometers or laser-Doppler anemometers (LDAs).^{26,27} While thermal anemometers and LDA provide high temporal resolution, the statistics are limited to a single point. A more robust method of obtaining turbulence statistics is using planar imaging techniques such as PIV and planar laser-induced fluorescence (PLIF) that yield two-dimensional velocity and concentration fields, respectively. Independently, PIV and PLIF techniques have been used to extract the velocity and density fields from the flow. However, a complete characterization of the turbulent mixing requires the simultaneous specification of *both* velocity and density fields. In essence, simultaneous PIV-PLIF measurements pave the way for the calculation of the complete two-dimensional stress tensors in turbulent mixing fields.

In this paper, a complete time series of concentration

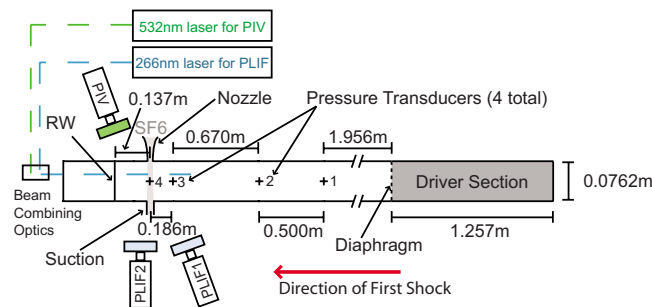


FIG. 1. (Color online) Schematic of the shock tube apparatus showing the nozzle, suction duct, the reshock wall (RW), pressure transducers, and the PIV and PLIF cameras. The camera labeled PLIF1 is used for recording the initial condition and early time evolution up to $90 \mu\text{s}$, while the PLIF2 camera is synchronized to the PIV camera.

maps showing the evolution of RM instability in a varicose gas curtain with and without reshock are presented. We characterize the initial conditions by performing calibrated PLIF measurements, providing input data that can be used in numerical simulations. We discuss the mixing width evolution for the cases of single shock and reshock, and provide a modified model for the nonlinear growth rate of perturbations after first shock. We then investigate the onset of turbulence and the mixing enhancement induced by the reshock wave by presenting the first simultaneous PIV-PLIF measurements obtained in RM mixing flows thus far.

II. EXPERIMENT

A. Experimental facility

The experiments presented in this paper are performed in a horizontal shock tube with a 3 in. square cross section that uses nitrogen as the driver gas and air as the driven gas (Fig. 1). A Mach 1.2 shock wave is generated by the rupture of a polypropylene diaphragm, that separates the nitrogen [at ~ 15 psi(gauge)] from the driven air (at an atmospheric pressure of 0.79 bar), using a plunger mechanism tipped with blades. Preshock waves were avoided by using a single diaphragm reinforced with tape. An adjustable Plexiglas reshock wall with an optical window that is transparent to both 266 and 532 nm light is located near the downstream end of the shock tube, to reflect the first shock.

Once generated, the shock wave travels down the shock tube to impinge upon a gravity-driven curtain of SF_6 flowing from a nozzle that exits through the top wall of the shock tube. The nozzle in the present experiments consists of a row of 21 cylindrical holes of 3.0 mm diameter and 3.6 mm separation that extends across the width of the shock tube. Diffusion of the flowing gas after it exits the nozzle creates a thin curtain with varicose perturbations imposed upon its outer layers. The flowing heavy gas exits the test section through a duct attached to the bottom wall of the shock tube. The duct is maintained at a small negative pressure just sufficient to remove all of the flowing gas. It should be noted that results from a recent simulation²⁸ suggest the three dimensionality of the flow after first shock (and by inference, after reshock) despite the nominally two-dimensional initial condition.

The shock driven RM instability is imaged at 25 times after shock impact using PLIF, including 15 times prior to the reshock time, $t=600 \mu\text{s}$, and five times after $t=600 \mu\text{s}$ in each of the singly shocked and reshocked cases. The PLIF images are complemented by combined PIV-PLIF measurements at two times before and after reshock. The heavy gas is mixed with acetone vapor for PLIF measurements. The acetone vapor is generated by bubbling SF_6 through liquid acetone in a bath maintained at 20°C . The flow is seeded for PIV with glycol droplets of $0.5\text{--}1.0 \mu\text{m}$ mean diameter generated by a fog machine. The output beam from a dual-head, frequency-quadrupled Gemini Nd:YAG (yttrium aluminum garnet) laser ($\lambda=266 \text{ nm}$) is shaped as a light sheet of thickness less than 0.5 mm and is used to illuminate the acetone in the SF_6 layer, to induce a broadband fluorescence in blue with a broad peak at 420 nm.²⁹ The fluorescence is captured using an Apogee 8P camera with a 1024×1024 charge coupled device (CCD) array operated with no binning. Another Apogee 32ME camera with a 2184×1470 CCD array and operated with 3×3 on-chip binning is used to provide optical access to regions not covered by the first camera (including the initial condition). Each camera is equipped with a Tamron SP Macro lens with a focal length of 90 mm resulting in spatial resolutions of 54.5 and $46.4 \mu\text{m}$, respectively. The contamination of the fluorescence signal by the light scattered off the glycol particles is prevented by using sharp visible-light interference filters [full width at half maximum (FWHM) ($=10 \text{ nm}$)] in front of each PLIF camera.

Illumination for the PIV images is provided by a dual-head, frequency doubled Nd:YAG laser operating at 532 nm. The beam from the laser head is shaped into a planar sheet of thickness less than 0.5 mm and combined with the PLIF beam prior to entering the shock tube. The combined beam path is parallel to the top wall of the shock tube, and is directed toward a measurement location located 20 mm below the nozzle exit. The light scattered off the glycol particles is imaged by a Kodak Megaplug ES 4.0/E cross-correlation camera with a 2048×2048 CCD array. The background fluorescence due to the acetone seeding is removed by using a Raman notch filter (centered at 532 nm with FWHM=17 nm) in front of the lens. Using this configuration, each experimental run produces a pair of PLIF images and a single velocity vector field. By choosing suitable timings on the PLIF and PIV lasers, *simultaneous* PIV-PLIF images are produced.

The PIV vectors are obtained by cross correlating the raw images using the software PIV SLEUTH.³⁰ A first correlation window of size 24×24 pixels and a second correlation window of size 32×32 pixels are used with suitable offsets for interrogations. A 50% overlap of the windows and a mild Gaussian smoothing ($\sigma=1$ over a 3×3 neighborhood) of the interrogated field are employed to increase the spatial resolution of the measurement, and to reduce the random noise, respectively. The rotation of the PIV and PLIF1 cameras (Fig. 1) results in a capture of distorted images. The distortions are corrected using a least-squares fit of the projective transform of a Cartesian grid imaged through the tilted cameras at the measurement location. The projective transform

accounts for the camera rotations about all three axes allowing the mapping of the PIV vectors to the PLIF fields to create a simultaneous concentration-velocity map of the flow. The maximum error in the mapping of the velocity vectors to the concentration field is less than ± 0.5 pixels ($\pm 27.3 \mu\text{m}$). It should be noted that the images captured by the PLIF2 camera remains undistorted and are used for calculating the density fields in the simultaneous PIV-PLIF measurements presented in this paper.

The intensity calibration of the PLIF images is performed using a specially coated nozzle to reduce spurious scattering from the laser beam. The nozzle flows 100% SF_6 -acetone mixture, and is placed just above the laser light sheet during calibration. Since the calibration is dependent upon the shot-to-shot variations of the PLIF laser intensity (measured to be $\pm 10\%$ with a Gaussian distribution), a Pyroelectric Joulemeter (Coherent J25LP-3) is used to compensate for the relative intensity variations between the calibration and the actual measurements during every shot.

Aberrations introduced into the PIV and PLIF images due to refractive index variations caused by the mixing of the air and SF_6 are expected to be negligible. Using the Gladstone–Dale equations, the maximum relative change in the refractive index is 7.2×10^{-5} for air, and 3.4×10^{-4} for pure SF_6 . The maximum relative distortion due to this refractive index variation (calculated as the ratio of the deviation of a light ray emanating from the region of interest to its angle in the absence of refractive index variations) is less than 0.0012 for viewing angles of less than 30° .

The triggering of the lasers, cameras, and other electronics is controlled by four pressure transducers (labeled 1–4 in Fig. 1) located along the shock tube and sampled at 10×10^6 samples/s. The signals from the pressure transducers located closest to the initial condition are used to measure the velocity of the first shock and the reshock waves.

B. Stability of a confined gas curtain

The instability associated with planar jets exiting into a sudden expansion or cavity is well known.^{31–33} A similar jet-cavity configuration is created by the SF_6 curtain flowing into the driven section of the shock tube. The shear stress at the interface between the curtain and the surrounding air creates two dominant counter-rotating vortices on either side of the curtain. The counter-rotating vortices destabilize the curtain and result in a weak wavering motion of the curtain in the streamwise direction. Thus, despite the elimination of ambient fluctuations, the motion of the curtain due to this hydrodynamic instability presents slightly different initial condition to the incoming shock wave during each run of the experiment. Depending on the phase of the oscillatory motion at shock impact, a slightly different pattern of evolution emerges.

A dramatic improvement in the stability of the curtain is achieved in the present experiments by the addition of two manifolds on either side of the nozzle. This novel nozzle design results in the mitigation of the shear stress at the jet edges by creating a coflowing air- SF_6 -air configuration

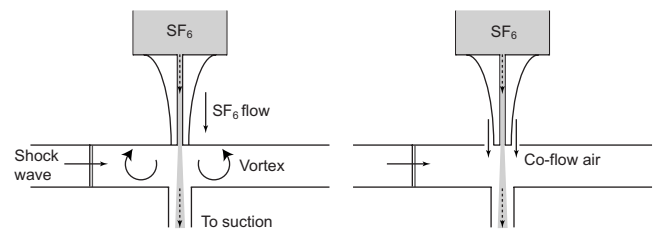


FIG. 2. Schematic of (left) original nozzle design and (right) new nozzle design with passive coflow.

(Fig. 2). The coflowing pattern weakens the counter-rotating vortices in the shock tube resulting in the exclusive development of sinuous structures during each shot of the experiment without the occurrence of downstream and upstream modes observed in the previous experiments. Further, the stable curtain also provides a high degree of shot-to-shot repeatability as evidenced by a comparison of the maximum spread in the width measurements between a previous experiment ($\pm 25\%$ at a time between 700 and 900 μs in Jacobs *et al.*¹⁴) and the current experiment ($\pm 5\%$ at 715 μs). Photographs of the nozzle and a fog-visualized stable curtain are shown in Fig. 3.

Another novel feature of the current experiments in the use of stereolithographic (STL) techniques for nozzle manufacture. While previous experiments used conventional machining techniques to machine their nozzles, resulting in severe constraints on the nozzle shapes, improvements in the strength of polymer resins have now paved the way for the STL manufacture of nozzles that are strong enough to withstand repeated Mach 2.0 impacts. For example, the present nozzles are made of SLA Accura-60-HR material and manufactured using STL techniques to an accuracy of a few microns. The primary advantage of using such modern manufacturing techniques for RM experiments is the possibility of creating almost any initial condition and modal compositions

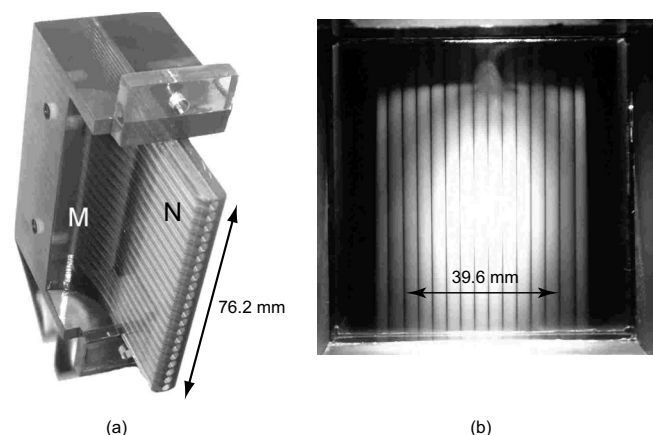


FIG. 3. Photograph of (a) the stereolithographically manufactured nozzle (n) showing the inlet manifolds (m) that result in the coflow. (b) End-view visualization of the gas curtain seeded with fog particles.

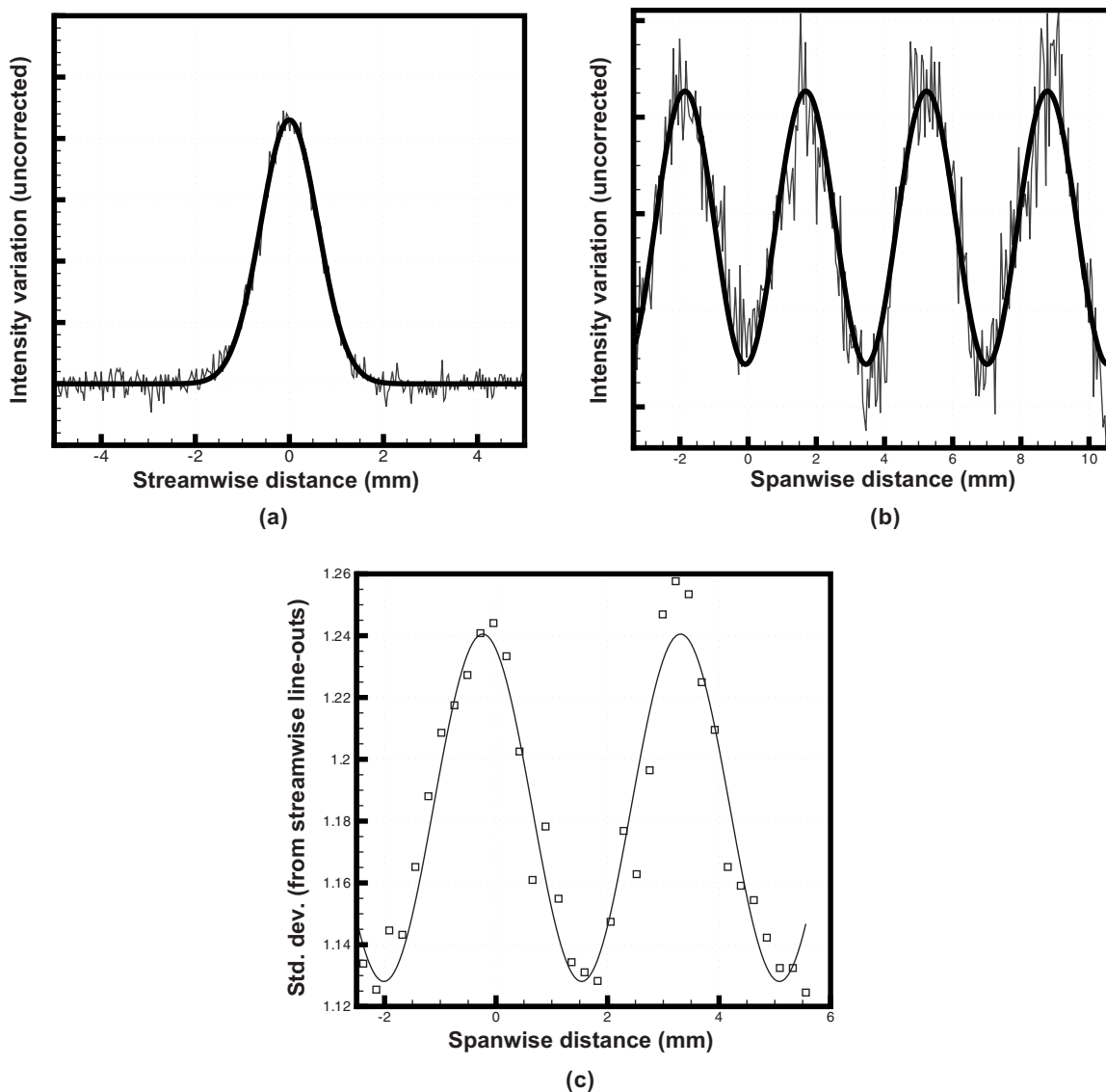


FIG. 4. (a) Intensity variation of initial conditions in the streamwise direction at the location of an intensity maximum (nozzle centerline). (b) Intensity variation in the spanwise direction along the nozzle centerlines. (c) Variation of the standard deviation of the widths at various spanwise locations. Thick solid lines represent curve fits to Eq. (1) with R^2 values of 0.98, 0.85, and 0.92, respectively.

that are, at best, difficult to generate in other membraneless apparatuses.

C. Characterizing the initial conditions

The varicose curtain in the present experiments is created by the advection-diffusion of a row of SF_6 cylinders emanating from the nozzle. While an exact solution can be written for the pure-diffusion problem of the row of cylinders by superposition of solutions from individual cylinders,³⁴ it is found that the pure-diffusion solution overestimates the peak concentration significantly. The best match to the experimentally measured intensity profiles is provided by Eq. (1), first used by Mikaelian:¹⁶

$$I = \frac{A(1 + B \cos kx)}{1 + B} e^{-y^2 \alpha^2 / (1 + \beta \cos kx)^2}. \quad (1)$$

The accuracy of this approximation is evaluated using

extracts of the intensity profiles from the initial condition (IC) images in the spanwise (x) and streamwise (y) directions. A comparison of the experimental intensity profile (extracted along a line oriented in the streamwise direction and passing through the point of maximum intensity) with a best-fit Gaussian curve (solid line) is shown in Fig. 4(a). It is clear that the streamwise intensity variation closely follows a Gaussian profile. In the spanwise direction, the variation of the intensity in the PLIF images is biased by the laser light-sheet intensity variations. After the elimination of this variation using polynomial curve fits, the concentration profile (extracted along a line oriented in the spanwise direction and passing through the points of peak intensity) follows a cosine function as shown in Fig. 4(b). The variation of the standard deviation of the Gaussian fits in the streamwise extracts of the intensity, due to the dependence of the diffusion on the peak concentration, is represented by the $1 + \beta \cos kx$ term in

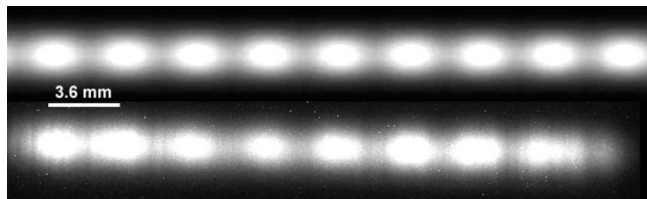


FIG. 5. An overlay of idealized initial conditions (above) and the experimentally imaged initial conditions (below) showing the contamination of the experimental image by laser light-sheet intensity variations, and other blemishes in the optical path.

Eq. (1). Despite the higher noise observed in the curve fits associated with the width variations, they follow a general pattern of cosine variation [Fig. 4(c)].

It follows from the profiles plotted in Fig. 4 that synthetic initial conditions created using fits to experimental data closely reflect actual experimental initial conditions with the distinct advantage of eliminating random noise present in the experimental images. The random noise has the potential to create spurious impulse density gradients during simulations that are absent in the experiments. Further, curve-fitted ICs serve to impose symmetry conditions that are present in the experiments but are masked in the captured images by the light-sheet intensity variations and other optical flaws. Finally, ICs of a higher resolution could be generated with a smaller error using curve fits than by the direct interpolation of experimental data. A comparison of idealized initial conditions based on the described fitting procedure with experimental data is shown in Fig. 5. The improvement in the quality of initial conditions in the synthetic ICs over the raw experimental ICs is clear. The list of parameters that specify the initial conditions for the current experiments according to the analytical expression in Eq. (1) is provided in Table I.

D. Mean convection velocity

The mean concentration of SF₆ imaged within each pixel is proportional to the intensity recorded in that pixel. Thus, the center of mass (CM) of the evolving RM structure can be calculated from the PLIF images. The errors in this calculation due to spurious background lighting variations are minimized by subtracting the backgrounds from each image prior to the calculation. The errors due to the thermal and shot noise are minimal due to the large number of pixels that are

TABLE I. List of parameters that specify the initial conditions for the current experiments. Coefficients correspond to Eq. (1), and the estimated errors represent 95% confidence intervals for the curve fits. All numbers are in SI units.

Parameter	Value
<i>A</i>	$3.2 \times 10^{-1} \pm 5\%$
<i>B</i>	$2.0 \times 10^{-1} \pm 5\%$
<i>k</i>	$1.75 \times 10^3 \text{ m}^{-1} \pm 3\%$
β	$-4.0 \times 10^{-2} \pm 10\%$
α	$8.36 \times 10^2 \text{ m}^{-1} \pm 0.5\%$

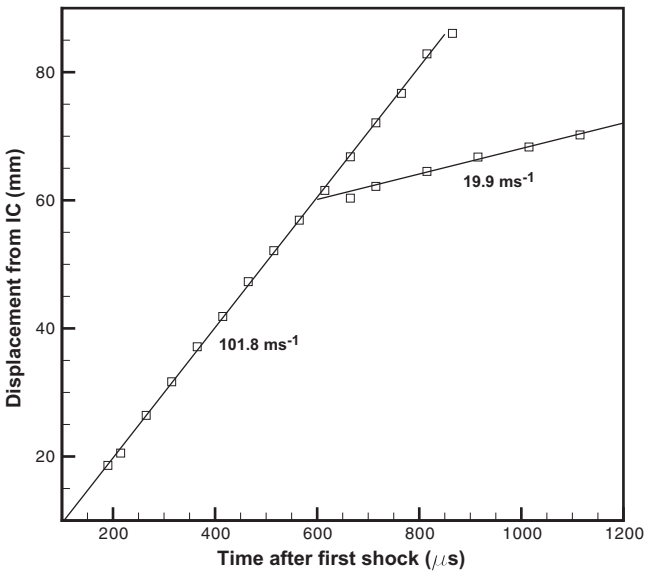


FIG. 6. Displacement of the unstable structure from the initial condition after first shock (a) and after reshock (r). Solid lines represent linear fits to the displacements. The size of the symbols represent maximum measurement error.

averaged. Conservatively, it is estimated that the error in the calculation of the streamwise CM location at each time is less than $\pm 300 \mu\text{m}$.

The linear variation of the CM location with time after the passage of the first shock and upon reshock is shown in Fig. 6. The structure is accelerated to a constant mean velocity within the first 100 μs of both the first shock and reshock. Further, signatures that result from the interaction of expansion waves with the developing RM instability are absent, pointing to the absence of contaminating expansion waves in the times investigated. In the case of a singly shocked RM instability, the CM of the structure begins to accelerate after the Mach 1.2 shock wave and quickly attains a constant mean velocity of 101.8 m s^{-1} . In the absence of a reshock, the structure continues to move with this linear velocity until late times. However, upon reshock at 600 μs , the structure decelerates to a constant mean velocity of 19.9 m s^{-1} . The nonzero value of the streamwise velocity after reshock merits further discussion. Estimates of the mean reshock velocity obtained from pressure traces yield a value of 323.5 m s^{-1} for the reshock velocity. This value is within 3% of the velocity obtained using one-dimensional gas dynamics calculations for a shock propagating in air through a SF₆ layer (332.3 m s^{-1}). Further, one-dimensional calculations performed to estimate the losses as the shock propagates through the layer of SF₆ resulted in an exit Mach number of 1.175 for an incident Mach number of 1.2. In addition, PIV measurements of the post-reshock mean velocity showed a value consistent with the estimates given in this paper. At this point, the reasons for the nonzero velocity after reshock are unclear, and it is possible that the boundary layer effects exert a significant influence on the post-reshock mean velocity. It is estimated that the error in the mean velocity associated with the linear fits is $\pm 1 \text{ m s}^{-1}$.

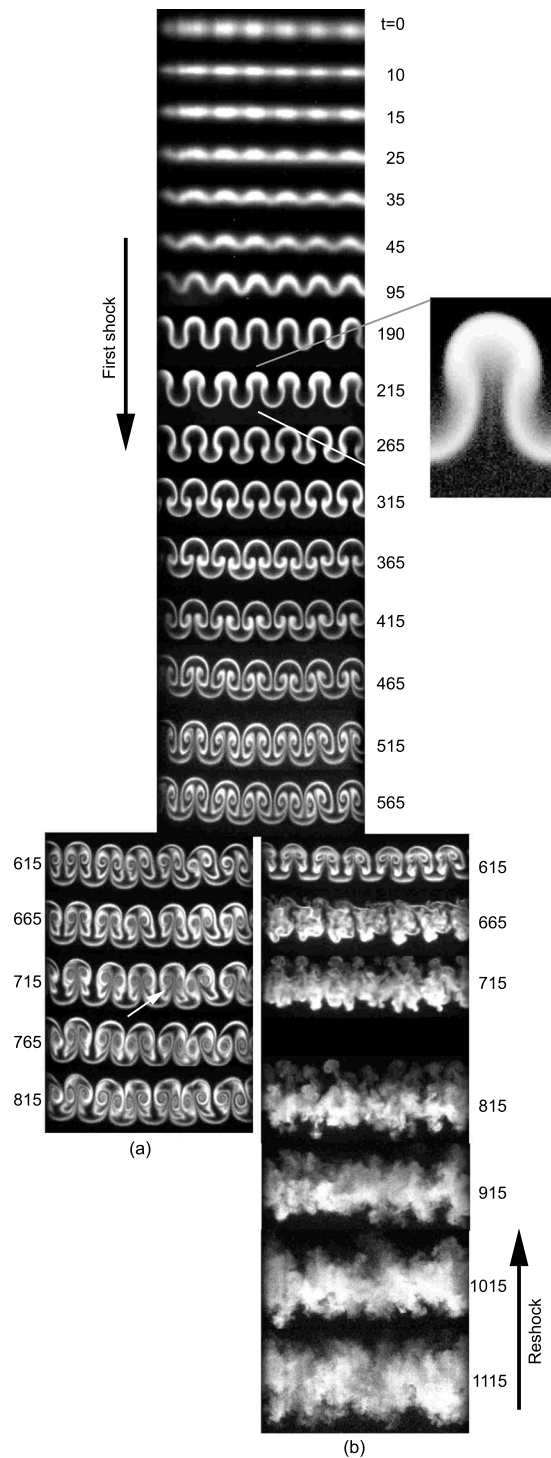


FIG. 7. Time series of RM instability development in a varicose gas curtain after first shock (left) and after reshock (right). The direction of the first shock and the reshock are marked by black arrows.

III. DISCUSSION

A. Time series

A time series of images capturing the evolution of the curtain upon impingement by a Mach 1.2 shock wave is shown in Fig. 7. The time series is a collage created from an ensemble of runs starting from nominally identical initial conditions. Since each run generates a pair of PLIF images at two different times, the consistency of the evolution patterns

between two runs of the experiment can be verified by using one image (at a fixed time) as a reference image. This method of building the ensemble time series by staggering the times provides a reliable way of capturing the evolution pattern without any bias due to small initial condition variations.

The upper section of Fig. 7 shows the evolution of the curtain prior to reshock time. The reshock wave arrives at $t = 600 \mu\text{s}$, after which two paths of evolution are presented. In the absence of a reshock, the evolution pattern follows Fig. 7(a). In comparison, the reshock wave changes the evolution to the pattern shown in Fig. 7(b). We now describe several features of the flow in both the singly shocked and reshocked cases. At time $t = 0 \mu\text{s}$, the shock wave is just upstream of the initial condition and about to strike the upstream interface. Upon striking the upstream interface, the transmitted shock wave traverses the curtain ($10 \mu\text{s}$), compressing it ($15 \mu\text{s}$) and depositing baroclinic vorticity at the interface. In these experiments, the postshock compression width is directly measured from the PLIF image ($15 \mu\text{s}$). While the upstream interface continues to grow, the downstream interface undergoes a phase inversion, reaches zero amplitude, and then grows along with the upstream interface ($25\text{--}35 \mu\text{s}$), as expected from the linear theory.¹² During this initial period of growth, projectiles of dense material that eject out of the primary structure in the downstream direction are created by the deformation of the shock wave as it traverses through the upstream interface (enlarged at $t = 215 \mu\text{s}$). These projectiles were first observed in gas cylinders by Kumar *et al.*,³⁵ and may become important in the mixing of multilayered fluids. After the initial period of growth, the symmetric curtain follows a sinuous mode of development ($190 \mu\text{s}$). During the nonlinear growth occurring between 215 and $515 \mu\text{s}$, mushroom structures emerge and develop in a manner that is qualitatively similar to those predicted by the vortex blob simulations of Rightley *et al.*²⁰ A minor up-down asymmetry, readily seen by inverting the image at $t = 365 \mu\text{s}$, is a consequence of three competing mechanisms: (a) the difference in the strengths of the shock wave impinging upon the downstream and upstream interfaces, (b) the time required for the phase inversion in the downstream interface, and (c) the enhanced vorticity deposition at the downstream interface (due to the higher misalignment between the pressure and density gradients created by the deformed shock wave).

In the absence of a reshock wave, the structures develop to later times without a clear transition to turbulence within the times investigated ($t \leq 815 \mu\text{s}$). The roll-ups at the vortex cores increase, and *pinching* structures develop just below the vortex cores (marked by arrow at $t = 715 \mu\text{s}$). The flow also begins to lose its spanwise symmetry as small non-uniformities in the initial conditions become important. However, large-scale structures of the order of the dominant wavelength remain prominent. In contrast, upon reshock at $600 \mu\text{s}$, an immediate dissociation of the larger scales into smaller scales occurs.

The passage of the reshock wave through a developed structure is shown at time $t = 615 \mu\text{s}$. The downstream bridges become flatter and the structure begins to be com-

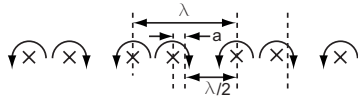


FIG. 8. Point vortex model for RM growth in a curtain for a nonuniform distribution of vortices of primary wavelength λ and offset distance a .

pressed. After the passage of the reshock wave, a dramatic increase in the mixing followed by a transition to a well-mixed state is observed. Interestingly, a phase shift of 180° in the location of peak material concentration is observed after reshock between the times $t=615$ and $665 \mu\text{s}$. While the vertical cross section of least material (at $615 \mu\text{s}$) is present in between the original centers of the nozzle cylinders, this cross section moves to the center of the nozzle cylinders at $665 \mu\text{s}$. Following these, $50 \mu\text{s}$ later, the structures become well mixed and the instability begins to lose its memory of initial conditions, as is evident from a comparison of the structures with and without reshock at $t=715 \mu\text{s}$. Vortex projectilelike structures observed by Zabusky and Zhang³⁶ are also found in the experimental images after reshock at $815 \mu\text{s}$. However, in the case of gas curtains at Mach 1.2, they are not consistent features, dissociate quickly, and are surmised to be the effect of small non-uniformities in the symmetric pattern prior to reshock. At even later times ($1115 \mu\text{s}$), the flow appears well mixed and visual evidence for the presence of the large-scale modes of the order of the primary wavelength is absent.

While reshock growth models do not exist for gas layers, analytical expressions for the nonlinear growth of RM instabilities after a single shock have been derived by Jacobs *et al.*¹⁴ (henceforth referred to as the Jacobs model). However, the present experiments violate one of the assumptions in the Jacobs model and hence necessitate a revision. In Sec. III B, we will derive the generalized form of the Jacobs model for the case of a row of stationary, nonequispaced, counter-rotating vortices applicable to shocked fluid layers created by the diffusive flow from a row of cylinders of arbitrary spacing.

B. Nonlinear growth rate

The nonlinear growth rate of the RM instability in a thin fluid layer was modeled by Jacobs *et al.*¹⁴ using a point vortex model consisting of a row of equispaced counter-rotating point vortices of identical magnitude. Using inviscid, potential flow theory, exact closed-form analytical equations were derived for the growth rates. In the present experiments, the ratio of the distances between the vortices was measured to be 1.17, violating the assumption of equal spacing. Thus, we derive a modified model that includes the effect of a nonuniform distribution of the counter-rotating vortices. We assume a vortex distribution as shown in Fig. 8. The symmetry inherent in the problem requires that the point vortices are of identical magnitudes despite their offsets.

Using series summations given in Lamb,³⁷ the streamlines for this configuration of vortices is given by

$$\psi = \frac{\Gamma}{2} \log \left[\frac{\cosh ky + \sinh kx}{\cosh ky - \sinh k(a+x)} \right]. \quad (2)$$

The streamwise and spanwise velocities induced by the vortices can be written (after simplification) as

$$V = -\frac{\partial \psi}{\partial x} = \frac{-k\Gamma[\cos kx + \cos k(a+x)]\cosh ky - \sin ak}{2(\cosh ky + \sin kx)[\cosh ky - \sin k(x+a)]}, \quad (3)$$

$$U = \frac{\partial \psi}{\partial y} = \frac{k\Gamma[\sin kx + \sin k(a+x)]\sinh ky}{2(\cosh ky + \sin kx)[- \cosh ky + \sin k(x+a)]}. \quad (4)$$

Following Jacobs *et al.*,¹⁴ let us look at the points where the U velocity vanishes to ease the integration. U vanishes when $kx + ka/2 = 0, \pm\pi, \pm 2\pi, \dots$. At these points, the V velocity is given by the following equations:

$$V = \frac{-2\Gamma \cos \frac{ak}{2} \cosh \frac{ky}{2} - \sin ak}{2 \left(\cosh ky - \sin \frac{ka}{2} \right) \left(\cosh ky \mp \sin \frac{ka}{2} \right)}. \quad (5)$$

Upon integration, we obtain the y location extremes of the interface to be solutions of

$$\begin{aligned} k^2 \Gamma t \cos \frac{ak}{2} + \sinh \frac{kw_o}{2} \pm \frac{kw_o}{2} \sin \frac{ak}{2} \\ = ky \sin \frac{ak}{2} \pm \sinh ky. \end{aligned} \quad (6)$$

The width of the curtain is now obtained as the difference between the solutions of Eq. (6). These equations reduce to the closed-form solution given by Jacobs *et al.*¹⁴ for $a=0$.

It is useful to examine the sensitivity of the curtain widths to the vortex offsets. A plot of curtain width (w), as a function of the offset phase (ak/π), is shown in Fig. 9. It is clear that small offsets create only small changes in the width of the curtain. In the present experiments, the phase offset is measured to be 0.078. Hence, Jacobs model and the general model given above do not differ significantly in their width predictions here. However, upon increasing the spacing between the cylinders (in the nozzle) to values much larger than those presented in this paper, the general model derived above is expected to perform better than the Jacobs original model. It should also be noted that the point vortex models are only used for data calibration and are derived using considerable simplifications including the assumption of point vortices driving the flow. They are not predictive in nature.

C. Effects of reshock: Growth rate amplification

The variation of the gas curtain width with time after first shock and the dramatic increase in the width upon reshock are shown in Fig. 10. The width after first shock is defined as the distance between the upstream and downstream locations of the structure where the peak concentration in a spanwise line-out reaches 5% SF_6 , and is calculated

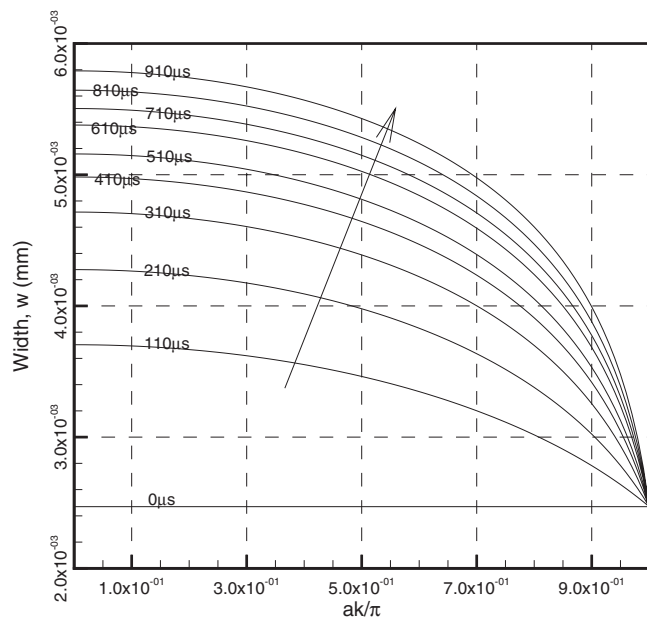


FIG. 9. Variation of the width (w) as a function of the vortex offset, ak/π .

as the average width measured over five adjacent wavelengths. The widths after reshock are calculated using the same thresholds but by averaging the intensities in the spanwise direction near the spanwise center of the structure. The contribution due to the small vortices propelled out at $t = 815 \mu\text{s}$ are neglected.

In the case of a singly shocked curtain, the shock compresses the curtain to a minimum postshock width of 2.47 mm at time $t = 15\text{--}30 \mu\text{s}$. After the initial period of compression, the width rebounds and follows the modified Jacobs model well up to $t = 800 \mu\text{s}$. The maximum error between the predictions of the model (obtained as a best-fit

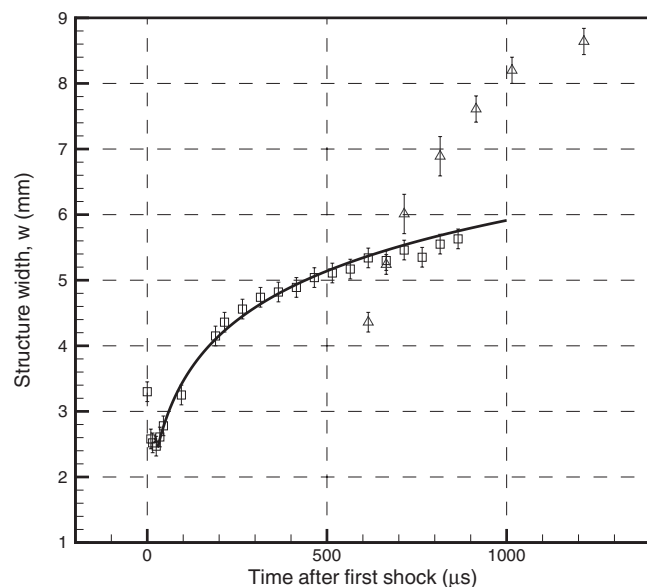


FIG. 10. Variation of the structure width (w) for the present curtain with (Δ) and without (\square) reshock. The solid line represents the modified Jacobs point vortex model.

curve of the experimentally measured widths) and the measured width was found to be $\pm 5\%$. While there is good agreement to the *form* of the Jacobs model, the value of the circulation that produces the best fit for the model ($\Gamma = 0.030 \text{ m}^2 \text{ s}^{-1}$) is quite different from the value of the circulation measured using PIV techniques ($\Gamma = 0.057 \pm 0.004 \text{ m}^2 \text{ s}^{-1}$). We now investigate the reasons for this discrepancy.

At a distance of 0.5 mm away from the vortex core, the azimuthal velocity induced is about 18 m s^{-1} . A particle moving at this distance from the vortex core is subjected to a centrifugal acceleration of roughly $65\,000g$, where g is the acceleration due to gravity. While the particles are subjected to tremendous acceleration, the Stokes number ($St = U_o D^2 / 18 \epsilon \nu_c R_o$, with $\epsilon = \rho_c / (\rho_p + 0.5 \rho_c)$, where U_o is the characteristic velocity of the fluid, D is the particle diameter, ρ_c is the density of the fluid, ρ_p is the particle density, R_o is the characteristic radius of the vortex, and ν_c is the fluid viscosity) of a fog droplet of $1 \mu\text{m}$ mean diameter is about 0.07.³⁸ Since the Stokes number is small, the asymptotic analysis given in Lasheras and Tio³⁹ is valid. Further, our region of interest is greater than $35 \mu\text{m}$ [$O(St)$] and less than $7200 \mu\text{m}$ [$O(St^{-1})$] away from the vortex cores and hence, the tracer particles accurately track the azimuthal fluid velocity.³⁸ Since the circulation depends only on the azimuthal velocity, it can be reasoned that the strong centrifugal forces are not the cause of this discrepancy.

A potential explanation arises out of the vortex blob simulations of Rightley *et al.*²⁰ It was found that deviations from the point vortex model using a vortex blob of finite size produced a significant reduction in the widths at a given time (Fig. 13 in Ref. 20). Hence, the assumption of a point vortex requires a smaller circulation than the actual value for correct width predictions, consistent with the present experiment. The observation that the widths follow the form of Jacobs model is in itself significant as a similar observation has been made at a higher Mach number of $Ma = 1.5$.⁴⁰ These results point to the possibility of scaling only the circulation term in the equations of the point vortex model keeping all the other terms the same.

We will now investigate the evolution of the reshocked structure. The reshock wave impinges upon the moving interface at roughly $600 \mu\text{s}$ and creates an immediate compression of the growing structure, as seen by the dip in the width around $t = 600 \mu\text{s}$. After shock passage, the width of the structure rebounds to values larger than the pre-reshock width. Further, the growth rate of the reshocked structure immediately after reshock ($15 \pm 3 \text{ m s}^{-1}$), calculated as a finite difference derivative of the measured widths, was found to be larger than the maximum growth rate after first shock ($7 \pm 3 \text{ m s}^{-1}$). This post-reshock growth rate is also substantially higher than the growth rate of the singly shocked curtain just prior to reshock ($1.7 \pm 0.5 \text{ m s}^{-1}$). Thus the reshock wave increases the mixing dramatically, and amplifies the growth rate of the RM instability as measured by the width metric.

This growth rate enhancement, however, is not unexpected and has been observed for the single interface case in numerous experiments^{1,2,24,25} and some simulations.^{41–43}

There is consensus that the amplification is dependent upon several factors including the reshock Mach number, the curvature of the evolving structure at the time of reshock, and the magnitude of the gradients encountered by the shock.⁴⁴ The curvature of the structure is, in turn, dependent upon the duration between the first shock and the arrival of the reshock. For example, in the present experiments, the reshock wave ($Ma=1.175$) encounters an already developing structure that presents a longer and far more convoluted interface for the deposition of baroclinic vorticity when compared to the interface presented by the initial condition to the first shock ($Ma=1.2$). The interaction of the shock wave with the longer interface is then expected to produce a greater vorticity deposition over a wider range of scales for a given density gradient. This additional energy injected into the developing structure by the reshock wave causes the enhanced growth rate and turbulent mixing.

D. Onset of turbulence upon reshock

In addition to the growth rate and width amplification upon reshock related to the largest scales of the flow, significant changes in the internal structure of the flow also occur. Rapid mixing, presumably produced by small vortices of varying scales, along with a dramatic redistribution of vorticity are observed. From the time sequence in Fig. 7, it appears that the mixing produced by the reshock wave in the 100 μs interval between 615 and 715 μs is greater than the mixing produced during the entire duration before reshock. In addition, the imprint of the large-scale structures is substantially reduced after reshock, as is evident from a comparison of the singly shocked and reshocked images at $t=815$ μs . This dramatic mixing is associated with large velocity fluctuations introduced into the flow by the reshock wave.

A histogram of the fluctuating streamwise and spanwise velocities, obtained from PIV measurements after reshock at 715 μs , is shown in Fig. 11. About 99% of the spanwise and streamwise fluctuation velocities fall between the ranges of ± 8.6 and ± 9.8 $m s^{-1}$ respectively. It is also interesting to note that the velocity fluctuations follow a roughly Gaussian profile with standard deviations of 4.9 and 4.8 $m s^{-1}$ in the streamwise and spanwise directions despite the developing nature of the flow. Finally, we observe that these velocity fluctuations are significant in comparison to the mean streamwise velocity of 20 $m s^{-1}$ but small compared to the local speed of sound.

E. Simultaneous PIV-PLIF

Snapshots of the simultaneous PIV-PLIF measurements obtained before and after reshock are shown in Figs. 12(a) and 12(b). The color contours represent volume-fraction concentration of SF_6 obtained using calibrated PLIF measurements after compensating for light-sheet intensity variations in the spanwise direction. In Fig. 12(a), the highest SF_6 concentration is present in the roll-ups around the vortex cores, and in the bridges formed from the material in between the vortex pairs from a single wavelength of the nozzle. This is expected as the maximum SF_6 concentration occurs at the

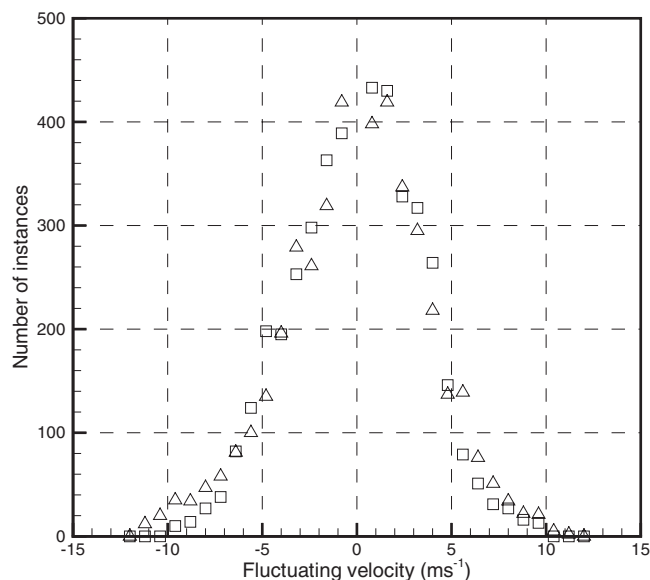


FIG. 11. Histogram of fluctuating streamwise (Δ) and spanwise (\square) velocities generated from a single PIV image after reshock.

center of the wavelength. After the counter-rotating vortices are formed in the curtain after first shock, the SF_6 near the vortices gets wrapped around, while the SF_6 in between the vortices gets pushed upstream by the induced velocity field. The pushing up of the heavy material is evident from the upward direction of the fluctuating velocity field in between the vortices.

After reshock, the ordered flow field is dramatically disturbed by the reshock wave [Fig. 12(b)]. A comparison of the concentration fields shows that the regions of peak concentration are advected downstream after reshock. Also, while the regions of high concentration occur midway across the upstream bridges before reshock, their location is offset in the spanwise direction by half a wavelength upon reshock. A comparison of the vector fields from images before and after reshock shows the sudden change in the nature of the flow. Small scale vortices have developed as a result of the reshock (as expected), due to the numerous regions of density gradients present prior to reshock. The induced motions of these vortices create an increase in the range of scales found within the flow.

The change in the flow structure can be better understood by an examination of the vorticity fields. Figures 12(c) and 12(d) show a comparison of the vorticity fields before and after reshock. The presence of a row of counter-rotating vortices with the bulk of the vorticity concentrated near the vortex cores is evident from Fig. 12(c). This spatial map of vorticity allows for the evaluation of the validity of the assumptions in the modified Jacobs model for the present (singly shocked) flow. The patches of positive and negative vorticity observed in Fig. 12(c) are reasonably close to a series of counter-rotating vortices, which is consistent with the good agreement in the shape of the model curve and the experimental data. However, the assumption of true point vortices is clearly not valid, suggesting that the results of Rightley *et al.*²⁰ mentioned earlier—that blobs of vorticity

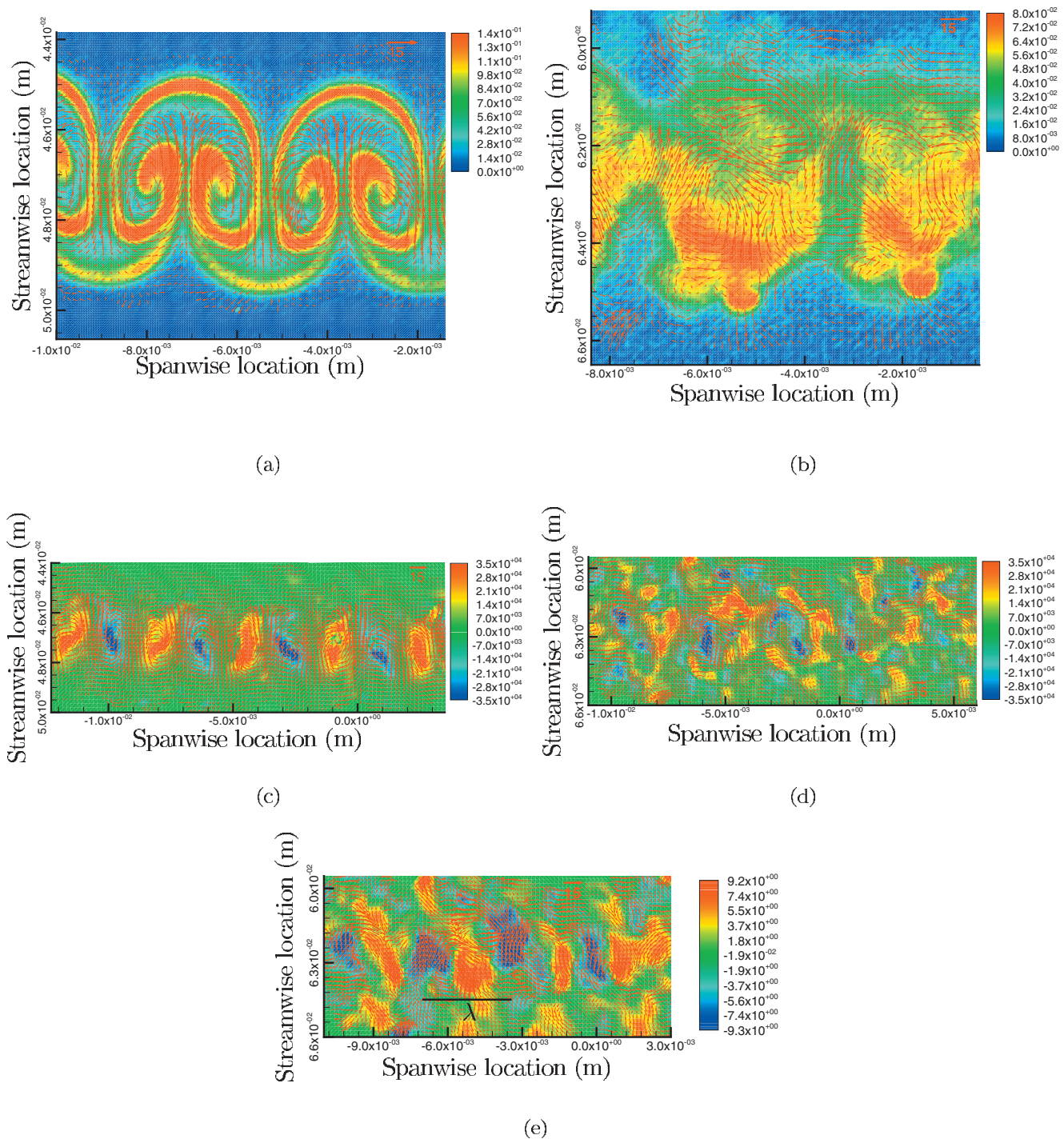


FIG. 12. (Color) [(a) and (b)] Simultaneous PIV-PLIF snapshots showing concentration contours and fluctuating velocity vectors (a) at $t=465 \mu\text{s}$ after first shock and (b) after reshock at $t=665 \mu\text{s}$. [(c) and (d)] Fluctuating velocity vector fields superimposed on vorticity contours showing the redistribution of vorticity after reshock. The images were taken at (a) $t=465 \mu\text{s}$ after first shock and (b) at $t=665 \mu\text{s}$ when reshock has occurred. (e) Contour plot of the fluctuating streamwise velocity showing the presence of modes of the size of the primary wavelength at $t=665 \mu\text{s}$. The vectors represent the fluctuating velocity. The solid line represents one primary wavelength.

can yield a lower growth rate than point vortices—indeed offer an explanation for the discrepancy in the estimate of the circulation using PIV measurements.

Upon reshock, we expect the baroclinic deposition of smaller scale vorticity throughout the structure, as suggested by the complex distribution of density gradients seen in Fig. 12(a). This vorticity would be expected to advect both the existing vorticity and concentration fields in a complex man-

ner, so that the ordered vorticity present in Fig. 12(c) gets redistributed throughout the reshocked structure. Spanwise symmetry is also not easily evident, suggesting an enhanced and evolving state of mixing after reshock at $t=715 \mu\text{s}$. The asymmetric distribution leads one to expect that the vortices advect each other in addition to the flow, complicating the evolution of the flow further. Prior to reshock, the mean positive circulation within the region of a single wavelength,

averaged over five wavelengths, is measured from the PIV data to be $0.059 \text{ m}^2 \text{ s}^{-1}$ and the mean negative circulation is measured to be $-0.055 \text{ m}^2 \text{ s}^{-1}$. After reshock, the mean positive and negative circulations increase to 0.099 and $-0.096 \text{ m}^2 \text{ s}^{-1}$, respectively, an increase of over 50%. The increase in the circulation and the emergence of the smaller scales is consistent with the observations of Schilling *et al.*⁴¹ in the case of a single interface with reshock. It should also be noted that the particle Stokes number after reshock is reduced to 0.03 due to the distribution of the vorticity over a larger area, resulting in an improved particle tracking fidelity.

While one might be tempted to conclude that the flow is turbulent based on the histogram shown in Fig. 11 and the vorticity plots, a contour of the fluctuating streamwise velocity in Fig. 12(e) shows the presence of large-scale structures of the order of the primary wavelength at $t=665 \text{ } \mu\text{s}$. Therefore, the time at which a reshocked structure becomes fully turbulent remains an open question.

IV. SUMMARY

For the first time, simultaneous PIV-PLIF measurements have been performed in RM flows to study the structure of concentration and velocity fields inside a singly shocked and reshocked air-SF₆-air fluid layer. Stable and repeatable initial conditions, achieved using a novel nozzle equipped with co-flowing ducts, have been characterized in detail using calibrated PLIF measurements. It is found that the initial conditions measured in the experiments agree well with the analytical predictions of Mikaelian,¹⁶ paving the way for highly accurate initial condition inputs for simulations.

The growth of the perturbations on the fluid layer upon interaction with a single shock, and its subsequent interaction with a reshock wave, have been captured in a collage created from an ensemble of runs starting from nominally identical initial conditions. Upon impact by a single Mach 1.2 shock wave, the perturbation widths grow in agreement with the form of an extended point vortex model even until late times. However, the circulation extracted from a best fit of the experimental widths to the model does not agree with the circulations measured directly using the PIV velocity vector field. It is argued that this apparent anomaly might be a consequence of the blob nature of the vortex deposition patterns.

The arrival of the reshock wave at $600 \text{ } \mu\text{s}$ brings dramatic structural changes to the layer, including increased width, increased circulation, growth rate amplification, emergence of smaller scales, redistribution of vorticity, enhanced mixing, and finally, a transition to turbulence-like conditions. The mean positive circulation (over each wavelength) increases from 0.059 to $0.099 \text{ m}^2 \text{ s}^{-1}$ (the magnitude of the negative circulation shows a similar increase). The reshock wave also increases the width of the mixing layer, and amplifies the instantaneous growth rate by roughly a factor of 4 from $1.7 \pm 0.5 \text{ m s}^{-1}$ to $7 \pm 3 \text{ m s}^{-1}$. Histograms of the streamwise and spanwise velocity fluctuations measured at $\sim 65 \text{ } \mu\text{s}$ after reshock follow roughly Gaussian profiles with standard deviations of 4.5 and 4.9 m s^{-1} , respectively. These velocity fluctuations are comparable to the mean velocity of

the structure (19.9 m s^{-1}) and create strongly turbulent conditions during the evolution of the structure after reshock.

ACKNOWLEDGMENTS

This work was supported by the Department of Energy under Contract No. DE-AC52-06NA25396.

- ¹M. Brouillette and B. Sturtevant, "Growth induced by multiple shock waves normally incident on plane gaseous interfaces," *Physica D* **37**, 248 (1989).
- ²M. Brouillette and B. Sturtevant, "Experiments on the Richtmyer–Meshkov instability: single-scale perturbations on a continuous interface," *J. Fluid Mech.* **263**, 271 (1994).
- ³J. W. Jacobs and J. M. Sheeley, "Experimental study of incompressible Richtmyer–Meshkov instability," *Phys. Fluids* **8**, 405 (1996).
- ⁴B. Puranik, "An experimental investigation of shock-induced interfacial instabilities," Ph.D. thesis, University of Wisconsin-Madison, 2000.
- ⁵J. D. Lindl, R. L. McCrory, and E. M. Campbell, "Progress toward ignition and burn propagation in inertial confinement fusion," *Phys. Today* **45**(9), 32 (1992).
- ⁶J. Yang, T. Kubota, and E. E. Zukoski, "Applications of shock-induced mixing to supersonic combustion," *AIAA J.* **31**, 854 (1993).
- ⁷W. D. Arnett, J. N. Bahcall, R. P. Kirshner, and S. E. Woosley, "Supernova 1987A," *Annu. Rev. Astron. Astrophys.* **27**, 629 (1989).
- ⁸K. O. Mikaelian, "Evolution of perturbations in shocked fluid layers," Lawrence Livermore National Laboratory Technical Report No. UCRL-JC-120826, 1995.
- ⁹J. W. Jacobs, D. L. Klein, D. G. Jenkins, and R. F. Benjamin, "Instability growth patterns of a shock-accelerated thin fluid layer," *Phys. Rev. Lett.* **70**, 583 (1993).
- ¹⁰J. M. Budzinski, R. F. Benjamin, and J. W. Jacobs, "Influence of initial conditions on the flow patterns of a shock-accelerated thin fluid layer," *Phys. Fluids* **6**, 3510 (1994).
- ¹¹J. M. Budzinski, R. F. Benjamin, and J. W. Jacobs, "An experimental investigation of shock-accelerated heavy gas layers," Los Alamos National Laboratory Technical Report No. LALP-95-012-110, 1995.
- ¹²K. O. Mikaelian, "Rayleigh–Taylor and Richtmyer–Meshkov instabilities in finite thickness fluids layers," *Phys. Fluids* **7**, 888 (1995).
- ¹³R. D. Richtmyer, "Taylor instability in shock acceleration of compressible fluids," *Commun. Pure Appl. Math.* **13**, 297 (1960).
- ¹⁴J. W. Jacobs, D. G. Jenkins, D. L. Klein, and R. F. Benjamin, "Nonlinear growth of the shock-accelerated instability of a thin fluid layer," *J. Fluid Mech.* **295**, 23 (1995).
- ¹⁵R. M. Baltrusaitis, M. L. Gittings, R. P. Weaver, R. F. Benjamin, and J. M. Budzinski, "Simulation of shock-generated instabilities," *Phys. Fluids* **8**, 2471 (1996).
- ¹⁶K. O. Mikaelian, "Numerical simulations of Richtmyer–Meshkov instabilities in finite-thickness fluids layers," *Phys. Fluids* **8**, 1269 (1996).
- ¹⁷P. M. Rightley, P. Vorobieff, R. Martin, and R. F. Benjamin, "Experimental observations of the mixing transition in a shock-accelerated gas curtain," *Phys. Fluids* **11**, 186 (1999).
- ¹⁸W. Rider, J. Kamm, P. Rightley, K. Prestidge, R. Benjamin, and P. Vorobieff, *Computational Methods and Experimental Measurements X* (WIT, Southampton, UK, 2001), Chap. 1.
- ¹⁹W. J. Rider, C. Zoldi, and J. R. Kamm, "How do numerical methods effect statistical details of Richtmyer–Meshkov instabilities?" Los Alamos National Laboratory Technical Report No. LA-UR-01-2833, 2001.
- ²⁰P. M. Rightley, P. Vorobieff, and R. F. Benjamin, "Evolution of a shock-accelerated thin fluid layer," *Phys. Fluids* **9**, 1770 (1997).
- ²¹P. Vorobieff, P. M. Rightley, and R. F. Benjamin, "Power-law spectra of incipient gas-curtain turbulence," *Phys. Rev. Lett.* **81**, 2240 (1998).
- ²²P. Vorobieff, P. M. Rightley, and R. F. Benjamin, "Shock-driven gas curtain: fractal dimension evolution in transition to turbulence," *Physica D* **133**, 469 (1999).
- ²³K. Prestidge, P. M. Rightley, P. Vorobieff, R. F. Benjamin, and N. A. Kurnit, "Simultaneous density-field visualization and PIV of a shock-accelerated gas curtain," *Exp. Fluids* **29**, 339 (2000).
- ²⁴S. G. Zaitsev, E. V. Lazareva, V. V. Chernukha, and V. M. Belyaev,

- "Intensification of mixing at the interface between media of different densities upon the passage of a shock wave through it," *Sov. Phys. Dokl.* **20**, 579 (1985).
- ²⁵M. Brouillette and B. Sturtevant, "Experiments on the Richtmyer–Meshkov instability: Small-scale perturbations on a plane interface," *Phys. Fluids A* **5**, 916 (1993).
- ²⁶F. Poggi, M.-H. Thorembey, and G. Rodriguez, "Velocity measurements in turbulent gaseous mixtures induced by Richtmyer–Meshkov instability," *Phys. Fluids* **10**, 2698 (1998).
- ²⁷L. Schwaedler, C. Mariani, G. Jourdan, L. Houas, and J.-F. Haas, "Shock-induced mixing zone characterization: an attempt by hot-wire diagnostic," *Shock Waves* **17**, 203 (2007).
- ²⁸V. G. Weirs, T. Dupont, and T. Plewa, "Three-dimensional effects in shock-cylinder interactions," *Phys. Fluids* **20**, 044102 (2008).
- ²⁹A. Lozano, B. Yip, and R. K. Hanson, "Acetone: A tracer for concentration measurements in gaseous flows by planar laser-induced fluorescence," *Exp. Fluids* **13**, 369 (1992).
- ³⁰K. T. Christensen, S. M. Soloff, and R. J. Adrian, "PIV Sleuth: Integrated particle image velocimetry (PIV) interrogation/validation software," University of Illinois at Urbana-Champaign Technical Report No. TAM 943, 2000.
- ³¹W. Cherdron, F. Durst, and J. H. Whitelaw, "Asymmetric flows and instabilities in symmetric ducts with sudden expansion," *J. Fluid Mech.* **84**, 13 (1978).
- ³²A. Maurel, P. Ern, B. J. A. Zielinska, and J. E. Wesfreid, "Experimental study of self-sustained oscillations in a confined jet," *Phys. Rev. E* **54**, 3643 (1996).
- ³³T. Kolsek, N. Jelic, and J. Duhovnik, "Numerical study of flow asymmetry and self-sustained jet oscillations in geometrically symmetric cavities," *Appl. Math. Model.* **31**, 2355 (2007).
- ³⁴J. Kevorkian, *Partial Differential Equations: Analytical Solution Techniques*, Texts in Applied Mathematics Vol. 35, 2nd ed. (Springer-Verlag, New York, 2000).
- ³⁵S. Kumar, G. Orlicz, C. Tomkins, C. Goodenough, K. Prestridge, P. Vorobieff, and R. Benjamin, "Stretching of material lines in shock-accelerated gaseous flows," *Phys. Fluids* **17**, 082107 (2005).
- ³⁶N. J. Zabusky and S. Zhang, "Shock-planar curtain interactions in two dimensions: Emergence of vortex double layers, vortex projectiles, and decaying stratified turbulence," *Phys. Fluids* **14**, 419 (2002).
- ³⁷H. Lamb, *Hydrodynamics* (Dover, New York, 1932).
- ³⁸A. Lecuona, U. Ruiz-Rivas, and J. Nogueira, "Simulation of particle trajectories in a vortex-induced flow: application to seed-dependent flow measurement techniques," *Meas. Sci. Technol.* **13**, 1020 (2002).
- ³⁹J. Lasheras and K.-K. Tio, "Dynamics of a small spherical particle in steady two-dimensional vortex flows," *Appl. Mech. Rev.* **47**, S61 (1994).
- ⁴⁰G. Orlicz, "Shock driven instabilities in a varicose, heavy-gas curtain: Mach number effects," M.S. thesis, University of New Mexico, 2007.
- ⁴¹O. Schilling, M. Latini, and W. S. Don, "Physics of reshock and mixing in single-mode Richtmyer Meshkov instability," *Phys. Rev. E* **76**, 026319 (2007).
- ⁴²M. Latini, O. Schilling, and S. S. Don, "Effects of WENO flux reconstruction order and spatial resolution on reshocked two-dimensional Richtmyer–Meshkov instability," *J. Comput. Phys.* **221**, 805 (2007).
- ⁴³M. Latini, O. Schilling, and S. S. Don, "High-resolution simulations and modeling of reshocked single-mode Richtmyer–Meshkov instability: Comparison to experimental data and to amplitude growth model predictions," *Phys. Fluids* **19**, 024104 (2007).
- ⁴⁴N. J. Zabusky, "Vortex paradigm for accelerated inhomogeneous flows: visiometrics for the Rayleigh–Taylor and Richtmyer–Meshkov environments," *Annu. Rev. Fluid Mech.* **31**, 495 (1999).